Catalysis Today xxx (2013) xxx–xxx

Contents lists available at ScienceDirect

Catalysis Today

journal homepage: www.elsevier.com/locate/cattod

Single-catalyst particle spectroscopy of alcohol-to-olefins conversions: Comparison between SAPO-34 and SSZ-13

Qingyun Qian[a], Javier Ruiz-Martínez[a,*], Mohamed Mokhtar[b], Abdullah M. Asiri[b,c], Shaeel A. Al-Thabaiti[b], Suliman N. Basahel[b], Bert M. Weckhuysen[a,**]

[a] Inorganic Chemistry and Catalysis, Debye Institute for Nanomaterials Science, Faculty of Science, Utrecht University, Universiteitsweg 99, 3584 CG Utrecht, The Netherlands
[b] Department of Chemistry, Faculty of Science, King Abdulaziz University, P.O. Box 80203, Jeddah 21589, Saudi Arabia
[c] Center of Excellence for Advanced Materials Research, King Abdulaziz University, P.O. Box 80203, Jeddah 21589, Saudi Arabia

ARTICLE INFO

Article history:
Received 5 July 2013
Received in revised form
16 September 2013
Accepted 25 September 2013
Available online xxx

Keywords:
Alcohol-to-olefins
Micro-spectroscopy
Acid strength
Acid site density
Coke formation
Chabazite

ABSTRACT

The formation of distinct hydrocarbon pool (HCP) species on individual micron-sized SAPO-34 and SSZ-13 crystals have been compared during methanol-to-olefins (MTO) and ethanol-to-olefins (ETO) conversion processes. In situ UV–vis micro-spectroscopy reveals the formation of 400 nm and 580 nm absorption bands, which are ascribed to poly-alkylated benzene (PAB) carbocations, the most active HCP species and poly aromatics (PA) the deactivating species, respectively. PAB formation within both catalysts is fitted with first-order kinetics at low reaction temperatures and activation energies (E_a) can be calculated, while PA/PAB ratio is calculated to monitor the deactivation process for different reaction temperatures. The results show that for both activation and deactivation processes, methylation reactions are leading in MTO and are controlled by acid strength; while olefins condensation reactions are governing in ETO and are affected more by acid site density. Moreover, the distribution of HCP species is visualized by confocal fluorescence microscopy, which demonstrates that the acid site density plays an important role on the local catalytic performance. Finally, synchrotron-based IR micro-spectroscopy reveals different activity of the two catalysts as shown by the intensity and frequency of distinct characteristic bands.

1. Introduction

Light olefins, such as ethylene and propylene, have been widely used as raw materials for the production of e.g. polymers [1,2]. However, the current high price of crude oil as well as more stringent environmental legislation have spurred great interests in developing new and improved catalytic technologies based on alternative feedstocks, such as methane and biomass. Among these processes, the conversion of alcohols (e.g. methanol and ethanol) to light olefins have received strong research attention [3,4]. Methanol can be produced from synthesis gas ($CO + H_2$), which can be obtained from almost any gasifiable carbon source, such as natural gas, coal, biomass and agricultural waste [5]. The methanol-to-olefins (MTO) process was discovered in 1976 and significantly improved by the discovery of the SAPO-34 material by Union Carbide [1,6]. Furthermore, the ethanol-to-olefins (ETO) process has received recent attention owing to the interest in the full utilization in the production and use of bio-ethanol, which can be obtained in large quantities from modern lignocellulosic biorefineries [1,7].

MTO and ETO processes can be efficiently catalyzed by various protonated zeolites or zeotype materials, among which SAPO-34 with large cavities (6.7 Å × 10.9 Å) interconnected through small windows (3.8 Å × 3.8 Å) is currently one of the archetypal industrial MTO catalysts, giving up to 80% total carbon yield of propylene and ethylene [8]. Moreover, the CHA topology is one of the few where both the silicoaluminophosphate (SAPO-34) and aluminosilicate (SSZ-13) analogs are readily synthesized [9]. It has been reported that SSZ-13 displays higher acid strength than SAPO-34 [10]. As a consequence, an enhanced production rate of olefins as well as aromatics retained in the catalyst pores was observed for SSZ-13, leading to a lower optimal temperature of operation [9].

Understanding the reaction mechanism and related deactivation pathways during catalytic processes are important topics as this knowledge can be further translated into designing new and improved catalyst materials. In the case of MTO, there is a general consensus that the reaction follows the hydrocarbon pool (HCP) mechanism, in which methanol is subsequently added to an organic scaffold [11–14]. While when using ethanol as a feed over H-ZSM-5, an almost identical product distribution is found as for the MTO

* Corresponding author. Tel.: +31 62 273 6379; fax: +31 30 251 1027.
** Corresponding author. Tel.: +31 30 253 4328; fax: +31 30 251 1027.
E-mail addresses: j.ruizmartinez@uu.nl (J. Ruiz-Martínez), b.m.weckhuysen@uu.nl (B.M. Weckhuysen).

0920-5861/$ – see front matter © 2013 Elsevier B.V. All rights reserved.
http://dx.doi.org/10.1016/j.cattod.2013.09.056

process. This suggests that ETO likely proceeds through similar HCP pathways [15]. Further investigations have shown that the trapped species within the zeolite channels after ETO are very similar than those found after MTO, although they contain a higher amount of ethyl-substituted molecules [16,17]. The formation of hydrocarbon species and their activity critically rely on the combination of reaction conditions, size of the cages/channels of the molecular sieves as well as the acid site density and strength [5,14,18,19]. However, active HCP species are often alkylated benzene molecules and their protonic counterparts [1,2,18,20]. Furthermore, these active species in SAPO-34 readily convert into larger aromatics that eventually block the active sites and hinder the diffusion of reactants as well as products [22,23]. Thus, the coke formation can affect the catalyst performance as it provokes variations in activity and selectivity. In the past decades, there have been intensive studies investigating the nature of the coke species and their formation mechanism by using of a variety of analytical tools, such as IR, UV–vis, electron spin resonance (ESR), nuclear magnetic resonance (NMR), gravimetrical (TEOM & TGA) and X-ray photoelectron spectroscopy (XPS) [24–27]. Nevertheless, the number of methods that allows the investigation of the coke formation under realistic reaction conditions is limited and even further diminishes when non-invasive methods or spatial resolution criteria are requested, which is crucial considering the dynamic nature of the catalyst system.

Recently, our group has reported that in the case of SAPO-34, the active aromatic species, alkylated benzene carbocations, follow different formation pathways during MTO and ETO by using a set of micro-spectroscopy techniques [21]. In this work, we extend this mechanistic approach for the study of individual SSZ-13 crystals, an aluminosilicate with CHA structure, stronger acid sites and in this specific case lower acid site density. We also include here an investigation of the formation of bulkier poly aromatic species, which are believed to deactivate the material. These results will be compared with SAPO-34 ones and after that, the role of acid strength and acid site density on the kinetics, location and nature of distinct hydrocarbon species during activation and deactivation in MTO and ETO processes will be assessed.

2. Experimental

2.1. Materials and experiments

The as-synthesized SAPO-34 and SSZ-13 materials under study have crystal sizes of $50 \times 50 \times 50\,\mu m^3$ and $40 \times 40 \times 40\,\mu m^3$, respectively. Their synthesis procedure has been reported elsewhere [28,29]. The Si/(Al + P) and Si/Al ratios are 0.204 and 17.7, which can be translated theoretically into two acid sites per cage for SAPO-34 crystals and two acid sites per three cages for SSZ-13 crystals. The crystals were placed on the heating stage of an in situ cell (Linkam FTIR 600) equipped with a temperature controller (Linkam TMS 93) where they were heated. During each measurement, the calcined crystals were first heated to 673 K at a rate of 15 K min^{-1}, then heated to 823 K with a rate of 5 K min^{-1}, and held at this temperature for 1 h under N_2 atmosphere. Subsequently, the temperature was brought to the required reaction temperature at a rate of 15 K min^{-1} after which the N_2 was flowing through methanol or ethanol thereby acting as carrier gas.

2.2. N_2 physisorption analysis

N_2-physisorption isotherms were recorded using a Micromeritics Tristar 3000 set-up operating at 77 K. Prior to physisorption measurements, all samples were degassed for 12 h at 573 K in a nitrogen flow. BET surface areas were determined using 10 points between 0.06 and 0.25. Micropore volumes ($cm^3\,g^{-1}$) were determined by *t*-plot analysis for *t* between 3.3 and 5.4 Å to ensure inclusion of all five minimum required pressure point.

2.3. Ammonia temperature programmed desorption

Acidity was investigated by temperature-programmed desorption (TPD) of ammonia under He flow (25 ml min^{-1}) using a Micromeritis Autochem II equipped with a TCD detector. 50 mg of catalyst was loaded and dried at 873 K for 1 h, then cooled down to 373 K. After that, pulses of ammonia were introduced up to saturation of the catalyst material. The TPD was performed up to 873 K with a heating ramp of 5 K min^{-1}.

2.4. In situ UV–vis micro-spectroscopy

The UV–vis micro-spectroscopy measurements were performed with an Olympus BX41 upright microscope using a 50×0.5 NA high working-distance microscope objective lens. A 75 W tungsten lamp was used for illumination. In addition, the microscope has a 50/50 double viewpoint tube, which accommodates a CCD video camera (ColorView IIIu, Soft Imaging System GmbH) and an optical fiber mount. A 200 μm core fiber connects the microscope to a CCD UV–vis spectrometer (AvaSpec-2048TEC, Avantes BV).

2.5. In situ confocal fluorescence microscopy

The confocal fluorescence microscopy studies were performed with a Nikon Eclipse LV150 upright microscope with a 50×0.55 NA dry objective lens. The confocal fluorescence microscopy images were collected with the use of a Nikon-Eclipse C1 head connected to the laser light sources (488 and 561 nm). The emission was detected with two photomultiplier tubes in the range 510–550 and 575–635 nm for the two lasers, respectively (in order to avoid channel overlap).

2.6. In situ synchrotron-based IR micro-spectroscopy

Synchrotron-based IR spectra were collected at beamline SMIS located at the French National Synchrotron SOLEIL (Paris, France). A Thermo Nicolet NEXUS 70 spectrometer, coupled to a Continuum XL microscope was used with the synchrotron light as the IR source. The microscope was equipped with a 15×0.5 NA Schwarzschild objective, a motorized *x* and *y* mapping stage and an adjustable rectangular aperture. For typical MTO and ETO measurements, the SAPO-34 crystals were placed in the in situ cell (Linkam FTIR 600) and heated up to 723 K in dry air (heating rate 15 K min^{-1}) for 30 min to activate the molecular sieves. Subsequently, the in situ cell was brought to reaction temperatures (15 K min^{-1}), and the alcohols were fed into the cell with several pulses. Spectra were collected during and after each pulse. For each measurement, the crystals were placed on a CaF_2 window located on the motorized (in *x*/*y*) mapping stage, recording the mid-IR (4000–1300 cm^{-1}) spectrum in transmission mode with a spectral resolution of 4 cm^{-1} and 32 or 16 scans co-added. An aperture of IR beam $20 \times 20\,\mu m^2$ was used to follow the MTO and ETO reactions in situ. Background measurements were performed with a spectral resolution of 4 cm^{-1} and 64 scans per spectrum.

3. Results and discussion

3.1. Textural properties and acidity of the materials

Table 1 summarizes the textural properties of the two materials under study, i.e., SAPO-34 and SSZ-13, as measured by N_2

Please cite this article in press as: Q. Qian, et al., Single-catalyst particle spectroscopy of alcohol-to-olefins conversions: Comparison between SAPO-34 and SSZ-13, Catal. Today (2013), http://dx.doi.org/10.1016/j.cattod.2013.09.056

Table 1
Textural properties of the large SAPO-34 and SSZ-13 crystals under study.

Sample	BET surface area ($m^2\ g^{-1}$)	Micropore volume ($cm^3\ g^{-1}$)	Mesopore volume ($cm^3\ g^{-1}$)
SAPO-34	492	0.229	0.010
SSZ-13	486	0.231	0.037

physisorption. The large SAPO-34 crystals are essentially microporous, which suggest that the crystals possess low defects content and the porosity is coming mainly from the microporous structure of the silicoaluminophosphate. In the case of its zeolitic counterpart, SSZ-13, despite most of the porosity originates from the microporous structure of the material, a certain amount of mesoporosity is observed, reflecting a less ideal and most likely more accessible material.

The ammonia TPD profiles of the large SAPO-34 and SSZ-13 crystals are presented in Fig. 1. The SSZ-13 and SAPO-34 materials show two distinct peaks at low and high temperatures. The ammonia desorption peak at around 423 K is ascribed to weak acid sites due to hydroxyl groups at the external surface of the material, therefore they are not related to the active species inside the cages of the molecular sieves [30,31]. The ammonia desorption peak at higher temperature corresponds to sites with stronger acidity, most likely due to Brønsted acid sites inside the cages. This peak is located at around 623 K for SAPO-34 and at around 688 K for SSZ-13. Two main conclusions can be drawn from the ammonia TPD results. First, the profiles clearly show that the SAPO-34 large crystals possess a higher amount of acid sites, and consequently a higher acid site density. This observation is in line with the theoretical values of two acid sites per cage for SAPO-34 and 0.66 acid sites per cage for SSZ-13. Second, the temperature difference between the second peak of desorption for SSZ-13 and SAPO-34 is indicative for a stronger acid sites in the former material, which is in line with literature data [10].

3.2. *In situ UV–vis micro-spectroscopy*

In order to fully compare the differences between SSZ-13 and SAPO-34, with respect to the activation and deactivation processes, in situ UV–vis micro-spectroscopy has been applied. During each MTO or ETO experiment, the micron-sized SSZ-13 and SAPO-34 crystals were heated to distinct reaction temperatures at which they were exposed to a flow of alcohol vapor. During the MTO and ETO reactions, pronounced color changes were observed over SSZ-13 and SAPO-34 crystals, which are indicative for specific chemical transformation processes. Fig. 2a and c presents a selection of optical micro-photographs of an individual SSZ-13 and SAPO-34 crystal taken throughout the MTO reaction at reaction temperatures of 528 K and 563 K, respectively. Due to the different reactivity of the two catalyst materials under study, they were evaluated at different temperatures to allow a better comparison [9]. For micron-sized SSZ-13 crystal, the color changes into yellow after 410 s, and the crystal subsequently turns into orange, and displays a brown color in the end. In contrast, when performing the same MTO on SAPO-34, a strong yellow coloration is observed along the edges of the crystal, with the highest color intensity after ~75 s on-stream. Subsequently, the crystal becomes more translucent, the fade rate being dependent on the reaction temperature [21,32].

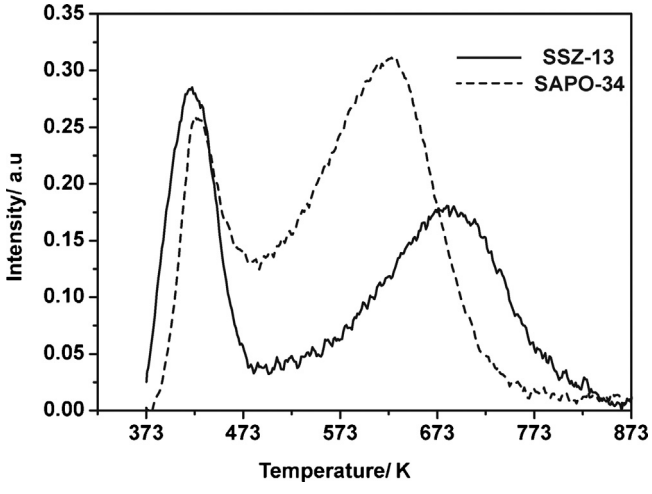

Fig. 1. Ammonia temperature programmed desorption profiles for the large SSZ-13 and SAPO-34 crystals under study.

To correlate the differences observed in the crystal coloration with changing reactivity, the corresponding spectra were recorded during each measurement, which were taken from a 2 μm spot in the central area of the crystals. As shown in Fig. 2b and d, the most prominent feature for both sets of UV–vis spectra is a strong absorption band located at around 400 nm, which is responsible for the yellow coloration and assigned to highly methylated benzenium carbocations [32,33]. With time-on-stream, the intensity of this absorption band starts to decrease drastically for SAPO-34 as shown in Fig. 2d, which is in line with the fading crystal color (Fig. 2c). Instead, in the case of SSZ-13, the intensity of the 400 nm absorption band decreases only to a small extent with time-on-stream (Fig. 2b). Furthermore, for longer reaction time, a second absorption band appears at around 480 nm and later on a weak and broad band rises at around 580 nm, which is particularly evident in the case of the more acidic SSZ-13 material, as reported previously [5].

The ETO performances of the micron-sized SSZ-13 and SAPO-34 crystals were also compared. Likewise, two different temperatures for the two catalyst materials are displayed, i.e., 461 K for SSZ-13 and 509 K for SAPO-34. As shown in Fig. 2e, the SSZ-13 crystal gradually turns from yellow to light brown with time-on-stream, while in the case of the SAPO-34 crystal, a faster coloration from yellow to dark orange was observed, as illustrated in Fig. 2g. Moreover, the colors for both catalyst materials during the ETO process are rather homogeneously distributed throughout the whole crystal, which is clearly different as compared to the MTO process. This observation suggests that the formation of HCP species follows different pathways during MTO and ETO, as shown in a recent work [21]. The corresponding UV–vis spectra are depicted in Fig. 2f and h. The absorption band at around 400 nm steadily grows for both crystals, however, the absorption band is increasing faster in intensity for SAPO-34. Moreover, an additional absorption band at around 500 nm becomes more evidenced at a later stage of the ETO reaction in the case of SAPO-34.

The large variety of carbonaceous species, formed during the MTO and ETO processes conducted on both SSZ-13 and SAPO-34 crystals, is clearly reflected in the complexity of the corresponding UV–vis spectra. For a reliable quantification of the intensities of the UV–vis absorption bands, we have developed and applied a systematic deconvolution procedure for both reactions over SSZ-13 and SAPO-34 at different temperatures [5,21,32,34]. Table 2 summarizes the Gaussian function dataset to deconvolute the UV–vis spectra obtained during MTO and ETO on SAPO-34 and SSZ-13. It is important to remark here that in all four cases under investigation, similar absorption band positions of the chosen Gaussian functions were required, which suggests a similar nature of the HCP species formed within the cages of both SAPO-34 and SSZ-13 crystals. This finding suggests that the nature of the HCP species is likely determined by the pore structure of the material. Five Gaussian bands, located at approximately 400, 448, 505, 580 and 670 nm, are necessary to reconstruct the experimental UV–vis spectra, whereas

Please cite this article in press as: Q. Qian, et al., Single-catalyst particle spectroscopy of alcohol-to-olefins conversions: Comparison between SAPO-34 and SSZ-13, Catal. Today (2013), http://dx.doi.org/10.1016/j.cattod.2013.09.056

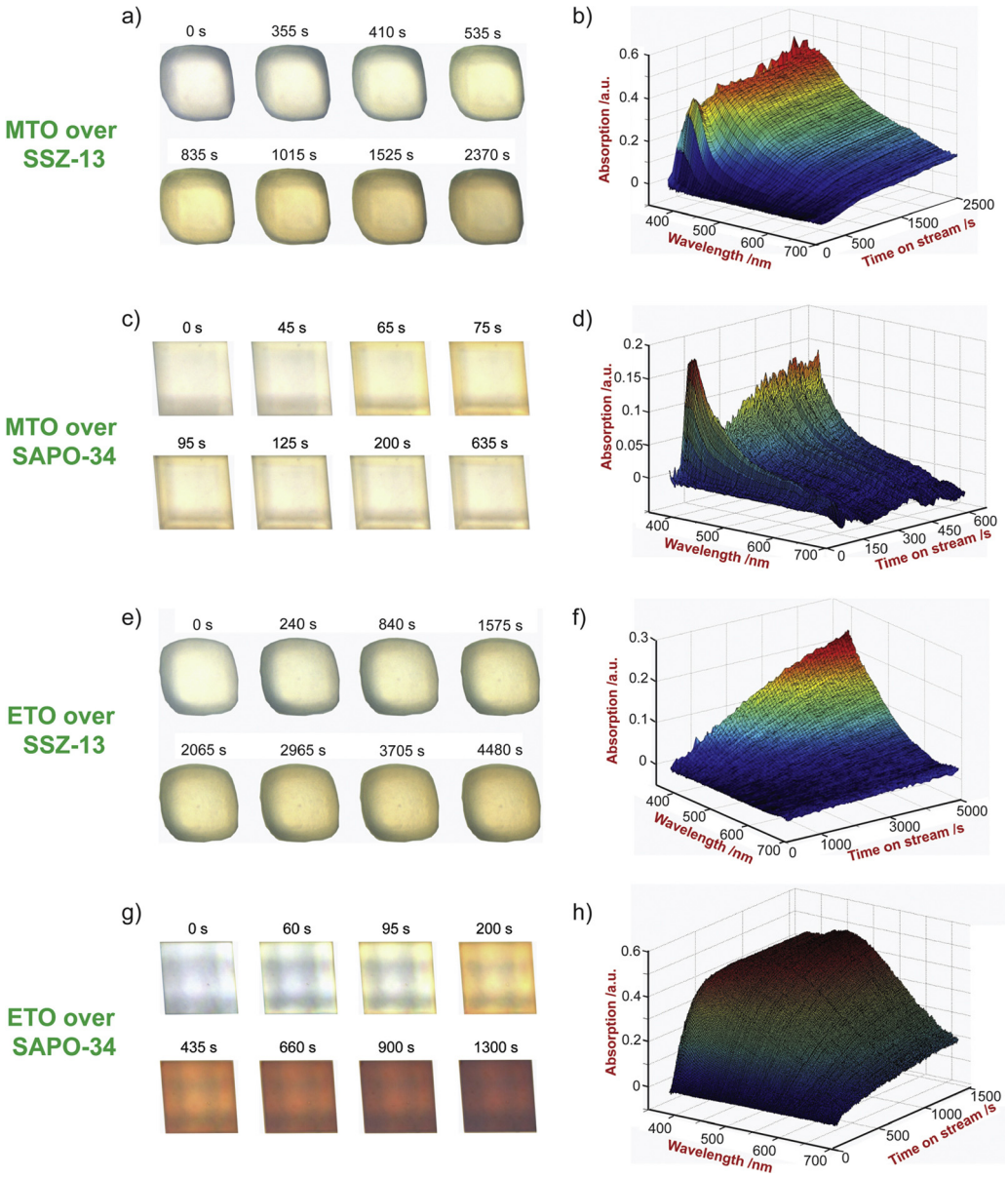

Fig. 2. Optical micro-photographs and corresponding UV–vis spectra during the methanol-to-olefins (MTO) reaction conducted at 528 K over an individual 40 μm-sized SSZ-13 crystal (a and b) and at 563 K over an individual 50 μm-sized SAPO-34 crystal (c and d) as a function of time-on-stream. The same for the ethanol-to-olefins (ETO) reaction conducted at 461 K over an individual 40 μm-sized SSZ-13 crystal (e and f) and at 509 K over an individual 50 μm-sized SAPO-34 crystal (g and h) as a function of time-on-stream.

a wide absorption band with a maximum at 700 nm is used to correct for the increasing baseline during the MTO and ETO reactions. Although it is not straightforward to assign each Gaussian band to one particular type of HCP species, our latest progress from both experimental data and theoretical calculations provides useful insight into the chemistry behind the deconvolution procedure [5]. More specifically, the 400 nm absorption band can be assigned to π–π^* transitions of poly-alkylated benzene (PAB) carbocations, which are considered to be the most active species during MTO reaction [13,32,35,36]. Bands with higher wavelengths can be rationalized in terms of an increased size of trapped alkylated aromatic compounds [21,34]. Furthermore, with the aid of state-of-art time-dependent DFT calculations combined with molecular dynamics (MD), it is now possible to assign these UV–vis bands in more detail [37]. Most of the single-ring aromatic cations contribute to the 400 nm band and bicyclic species containing up to four methyl

Table 2
Overview of the band positions and widths of the Gaussian functions used for the deconvolution of the in situ UV–vis absorption spectra for the methanol-to-olefins (MTO) and ethanol-to-olefins (ETO) processes over individual SAPO-34 and SSZ-13 crystals.

	Position and width (between brackets) in nanometers of the Gaussian functions					
MTO on SAPO-34	403 (31)	448 (42)	505 (46)	580 (50)	670 (65)	700 (800)
ETO on SAPO-34	405 (33)	448 (46)	510 (55)	590 (60)	675 (62)	700 (800)
MTO on SSZ-13	400 (31)	448 (45)	505 (48)	575 (60)	665 (65)	700 (800)
ETO on SSZ-13	405 (33)	448 (46)	510 (50)	585 (60)	670 (65)	700 (800)

Please cite this article in press as: Q. Qian, et al., Single-catalyst particle spectroscopy of alcohol-to-olefins conversions: Comparison between SAPO-34 and SSZ-13, Catal. Today (2013), http://dx.doi.org/10.1016/j.cattod.2013.09.056

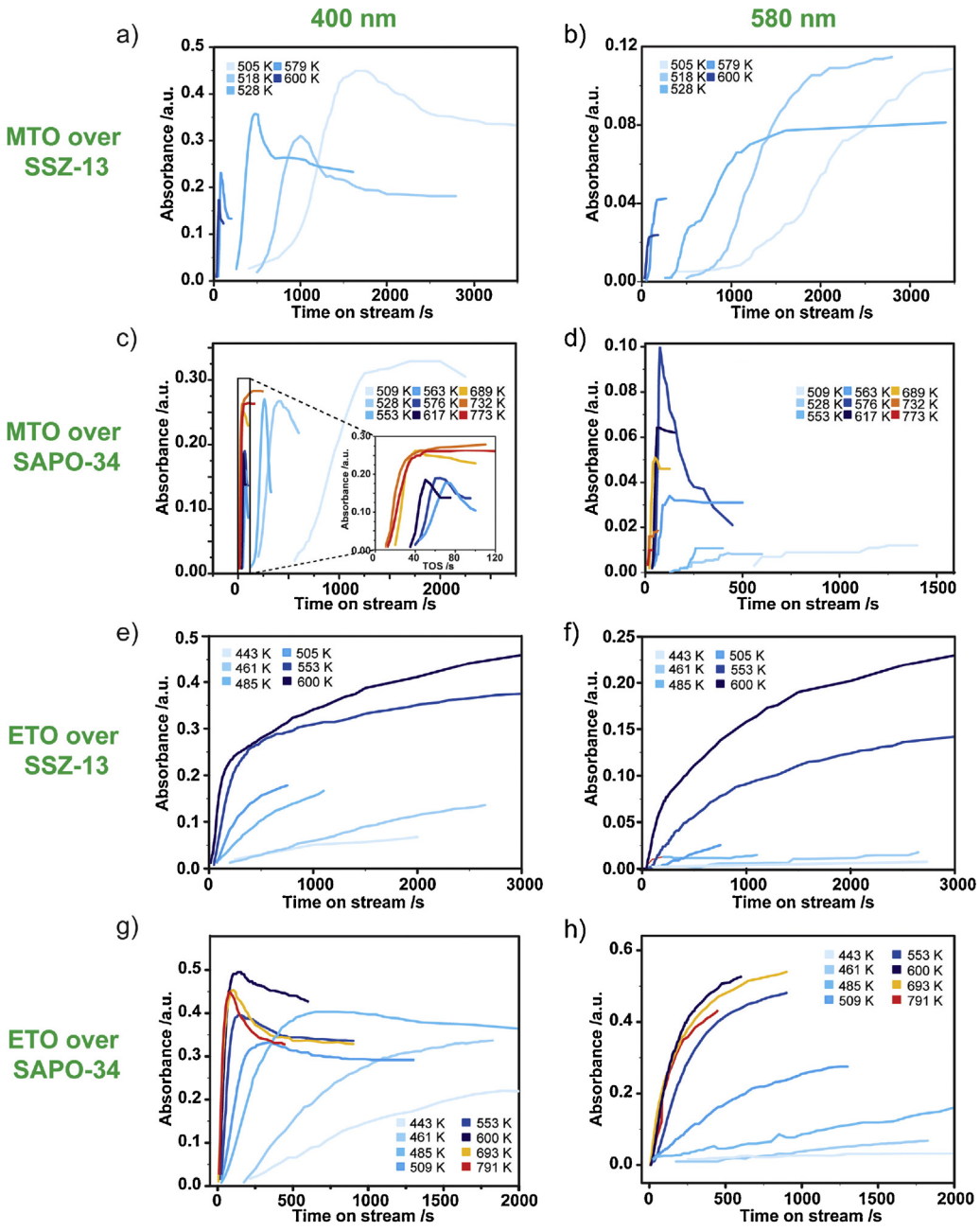

Fig. 3. Absorbance intensity of the Gaussian bands at 400 nm and 580 nm as a function of time-on-stream for the methanol-to-olefins (MTO) reactions over individual 40 μm-sized SSZ-13 crystals (a and b) and individual 50 μm-sized SAPO-34 crystals (c and d), for the ethanol-to-olefins (ETO) reactions over individual 40 μm-sized SSZ-13 crystals (e and f) and individual 50 μm-sized SAPO-34 crystals (g and h) at different reaction temperatures.

Source: Fig. 3c and g were adapted from Ref. [21].

groups show broader absorption bands extending to 450 nm, while heavier ones contribute to the absorption band around 505 nm. Additionally, the phenanthrenic species show high absorbance at longer wavelengths, in particular around 560 nm. Moreover, the largest ring system that can be accommodated in the cages is pyrene, which absorbs light at even longer wavelength. On the other hand, methylated naphthalenes only possess very limited activities toward olefins production and HCP species with a higher number of aromatic rings are no longer active [5,38,39].

By applying the above mentioned deconvolution procedure to the four sets of UV–vis absorption spectra obtained for the MTO and ETO reaction over individual SAPO-34 or SSZ-13 crystals, it has been possible to determine the absorbance intensities of the Gaussian curves at 400 and 580 nm at different reaction temperatures as a function of time-on-stream. The main reason to limit our discussion to these two Gaussian functions is because these two absorption bands are well resolved from each other and no band overlapping occurred. In addition, the 400 nm band is indicative for the most active HCP species, while the 580 nm band is representative for PA species, the deactivating HCP species. In other words, by monitoring the intensities of 400 nm and 580 nm bands we can directly assess the contributions of specific markers for active and deactivating species. The results of this spectroscopic approach are summarized in Fig. 3.

In the case of the 400 nm absorption band during the MTO process, as illustrated in Fig. 3a and c, it is evident that in the low temperature region (i.e., below 600 K for SSZ-13 and below 617 K for SAPO-34), the two crystals behave very similarly. First, the

Please cite this article in press as: Q. Qian, et al., Single-catalyst particle spectroscopy of alcohol-to-olefins conversions: Comparison between SAPO-34 and SSZ-13, Catal. Today (2013), http://dx.doi.org/10.1016/j.cattod.2013.09.056

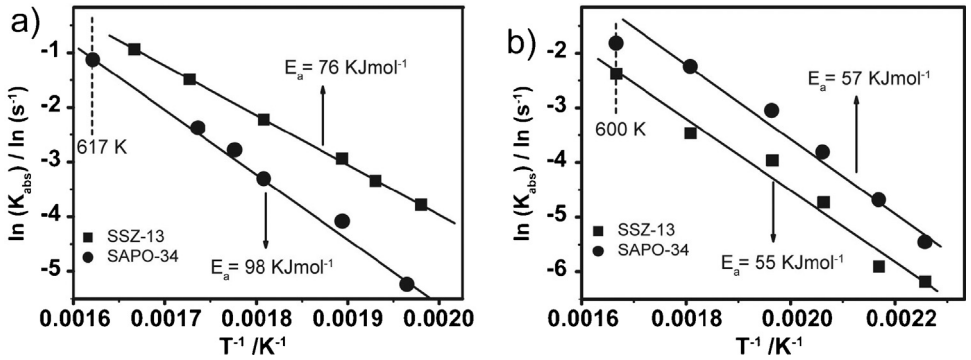

Fig. 4. Arrhenius plots of the fitted curves corresponding to the intensity profiles of the absorption band at around 400 nm obtained from the in situ UV–vis spectra measured on individual 40 μm-sized SSZ-13 crystals and individual 50 μm-sized SAPO-34 crystals during (a) the methanol-to-olefins (MTO) and (b) ethanol-to-olefins (ETO) reactions. Source: Data for MTO and ETO reactions on SAPO-34 crystal were taken from Ref. [21], data for MTO reactions on SSZ-13 crystal was taken from Ref. [5].

formation rate for the band of the active HCP species increases with increasing temperature. Second, for all temperatures in this region the intensity of this absorption band decreases after reaching a maximum. The similarities suggest a similar PAB formation path for the two crystals. In the case of the 580 nm absorption band during the MTO process, as illustrated in Fig. 3b and d, clear temperature differences exist when comparing the two crystals. More specifically, for SSZ-13 the intensity of this band is already very pronounced at the lowest reaction temperatures (i.e., 505 K and 518 K) as shown in Fig. 3b. While for SAPO-34, the growth of the 580 nm absorption band is very slow when the reaction temperature is below 553 K (Fig. 3d). Interestingly, the onset in the formation of the 580 nm absorption band corresponds with a drop of the 400 nm absorption band. This observation is more evidenced in the case of SSZ-13 with less acid site density (condensation of adjacent HCP species is thus avoided [27]), which is an indication that deactivating PA species are most likely formed from the active single-ring aromatics [1,2]. Furthermore, it was suggested by theoretic modeling that the side-chain methylation might be a deactivating route leading to coke precursors rather than olefins production [40]. Thus, the formation of PA species, as represented by the 580 nm absorption band, is likely based on methylation followed by condensation reactions of active PAB species.

In the case of the 400 nm absorption band during ETO over SSZ-13 and SAPO-34, as shown in Fig. 3e and g, it can be seen that faster kinetics takes place with increasing temperature in the reaction temperature window under study. Furthermore, the intensity of this absorption band slightly drops after reaching a maximum for SAPO-34, whilst for SSZ-13 a slow increase is observed. In the case of the 580 nm absorption band for ETO, the temperature dependency for the two crystals is the same, as the fact that a faster kinetics occurs for both crystals. Nevertheless, the intensity of this absorption band is much more pronounced for SAPO-34 as compared to SSZ-13, which might be due to its higher acid site density [41].

In order to analyze the data in more detail, time evolution profiles of the 400 nm absorption band from the above mentioned four sets of experiments were fitted into a first-order reaction. The procedure was reported in previous works [5,21]. More specifically, for each band the evolution of the maximal absorbance as a function of time was monitored at different temperatures. The rapidly increasing regions in the absorbance (A) versus time (t) curves (see Fig. 3a, c, e and g) that follow first-order kinetics were selected and fitted to the equation $\ln(A_{max} - A) = \ln(A_{max}) - k{\cdot}t$. Thus we corrected for an induction period at the beginning and for the occurrence of secondary reactions near the end of the process. For example, the regions between $0.2A_{max}$ and $0.5A_{max}$ for MTO over SAPO-34 and between $0.2A_{max}$ and $0.7A_{max}$ for ETO over SAPO-34 were used. Therefore, from this fitting procedure the rate constant k for each reaction temperature (T) can be determined. Consequently, the $\ln(k)$ as a function of $1/T$ is depicted in Fig. 4. The slope of these Arrhenius curves is denoted as the activation energy (E_a) of formation of the PAB carbocations responsible for the increase of the 400 nm absorption band in the UV–vis spectra. Moreover, the time interval (Δt) of the first-order reaction region is also used as a second method to determine the activation energy (E_a), as calculated from the slope of the $\ln(1/\Delta t) - 1/T$ plot.

In the Arrhenius plot, depicted in Fig. 4a and b, the activation energy (E_a) for the formation of PAB carbocations can be obtained from the slope of the curve. In the case of MTO reaction, the E_a for the formation of the 400 nm band is 98 kJ mol^{-1} for SAPO-34 and 76 kJ mol^{-1} for SSZ-13, as shown in Fig. 4a. These values show a strong correlation with the theoretical rates of methylation reactions, indicating that the methylation reactions are rate determining steps for the formation of PAB carbonations in both SAPO-34 and SSZ-13 crystals [5]. Furthermore, the E_a value is lower for SSZ-13, which is most probably due to its higher acid strength as suggested both experimentally and theoretically [5,9]. Another evidence for acid strength governing the PAB formation is that although SSZ-13 crystals possess a lower acid site density, it still exhibits a much faster formation rate in all measured temperatures as compared to SAPO-34 crystals.

In contrast, for ETO, the calculated E_a values for PAB formation, represented by the 400 nm absorption band, are rather similar when comparing the SAPO-34 and SSZ-13 crystals, which are 57 and 55 kJ mol^{-1}, respectively. Those E_a values are comparable to the E_a for the condensation of light olefins into aromatic species [21,42]. Furthermore as reported previously, it demonstrates that indeed ETO over SAPO-34 exhibits different mechanisms with respect to the generation of PAB carbocations at low temperatures as compared to MTO [21]. Hence, one would expect that the same reaction route holds for the ETO over SSZ-13 as compared to SAPO-34. The comparable E_a values for the SAPO-34 and SSZ-13 materials indicate that the acid strength does not play a major role with respect to the PAB formation for ETO. In other words, the acid strength does not influence the condensation of light olefins into aromatics to a large extent as this is the major route for the formation of PAB carbocations.

In order to monitor the deactivation of the crystals, the intensity ratios of the absorption bands at 580 nm and 400 nm band has been analyzed. Fig. 5 displays these ratios calculated at the reaction time when the 580 nm absorption band reaches a maximum. In the case of MTO, it can be deduced from Fig. 5a that a volcano type of curve in the measured temperature region exists for both catalyst materials. As PA species are most likely formed from methylation followed by condensation of PAB species as discussed above, this observed volcano type temperature-dependency can be rationalized by an "alkylation-dealkylation" equilibrium of aromatics as reported previously in ZSM-5 catalyst [43]. However, a maximum

Please cite this article in press as: Q. Qian, et al., Single-catalyst particle spectroscopy of alcohol-to-olefins conversions: Comparison between SAPO-34 and SSZ-13, Catal. Today (2013), http://dx.doi.org/10.1016/j.cattod.2013.09.056

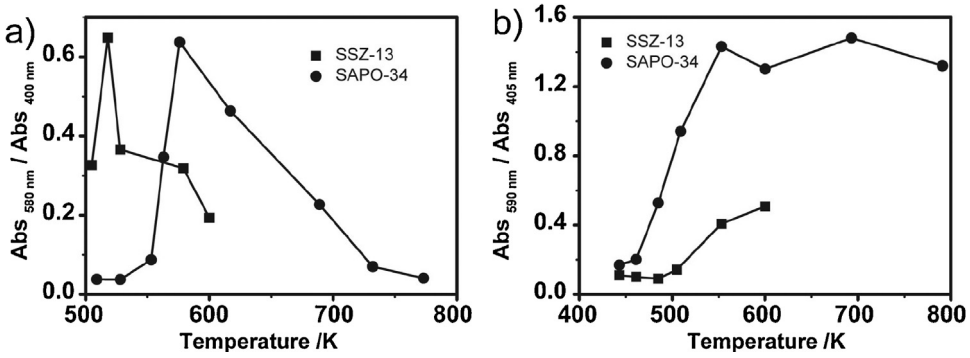

Fig. 5. Absorbance intensity ratios between the Gaussian band at ~580 nm and 400 nm as a function of reaction temperature taken (a) during the methanol-to-olefins reaction (MTO) and (b) during the ethanol-to-olefins (ETO) when the absorbance of the 580 nm band reaches a maximum.

of the intensity ratio occurs at 518 K and 576 K for SSZ-13 and SAPO-34, respectively. As the formation of different types of HCP species directly affect the performance of the catalyst materials, the shift of the observed temperature may strongly affect the operation temperature of the MTO reactions over SAPO-34 and SSZ-13 samples. This is in line with previous observations, where the optimum conversion capacity of SSZ-13 was shifted to lower temperature for about 50 K due to its higher acid strength [9]. Therefore, it seems very reasonable to conclude that it is the different acid strength that affects the methylation reactions, which induces a temperature shift in the optimum formation of different types of HCP species including both PAB and PA carbocations. Hence, a temperature shift in the optimum MTO performance can be obtained. Moreover, in the case of SAPO-34, the decrease in the ratio above 576 K means that the retained hydrocarbons contain less PA, which is in good agreement with previously reported results [9].

In the case of ETO, the ratio between the amount of PA species (deactivating species) and PAB carbocations (active species) increases with increasing reaction temperature for both catalyst materials until reaching a maximum, as illustrated in Fig. 5b. This is different from the volcano type of temperature-dependency behavior observed from MTO (Fig. 5a), which implies that there is no clear direct connection between the formation of PA and PAB species. In other words, "alkylation-dealkylation" equilibrium/reactions does not apply in the ETO process for formation of HCP species, at least not to a large extent. Instead, olefins condensation is more reasonable to contribute to the PA formation. Therefore, the higher ratios as well as the faster formation of HCP species (both PA and PAB molecules) (evidenced by Figs. 3f, 4h and 4b) for SAPO-34 at all reaction temperatures can be well explained. The reason is that higher acid site density favors condensation reactions as reported previously [27]. Thus, different from the case of MTO, the acid strength of a porous material is not the major factor for governing PA formation during ETO.

3.3. Confocal fluorescence microscopy

The spatiotemporal distribution of carbonaceous species within individual SSZ-13 crystals was monitored by confocal fluorescence microscopy as such species exhibit fluorescence in the visible light region. As a result, 2D and 3D maps of carbonaceous species can be constructed with sub-micrometer resolution [44,45]. Furthermore, the optical properties of the carbon species can be related to their molecular dimensions, where the more conjugated and extended compounds absorb light at higher wavelengths [32,34]. This allows us to discriminate between different coke species by exciting the sample with distinct laser lines. In this work, two different laser lines have been used; i.e., at 488 and 561 nm with the fluorescence detection region set at 510–550 and 575–635 nm, respectively.

Fig. 6 depicts a series of confocal fluorescence microscopy images in the middle plane of a single SSZ-13 and SAPO-34 crystals collected during MTO at 600 K and ETO at 509 K. The images show the combination of the light emitted upon excitation with the 488 and 561 nm lasers and illustrate the location of the less and more extended coke species (from green to red, respectively) [21]. It is important to note that this technique was used as an imaging tool and no quantitative information can be extracted from this study. This is due to the fact that the sensitivity of the fluorescence detectors for the two lasers might differ from each experiment because those settings were chosen for the best display of the fluorescence species. Therefore the evolution of the HCP species with respect to the size and distribution can be followed within one crystal. For MTO on SSZ-13 at 600 K, as shown in Fig. 6a, the formation of the fluorescent species is concentrated in the outer rim of the crystal and the light emitted goes from green to red with time-on-stream. This observation can be explained in terms of the formation of more extended HCP species. This is similar to the previous findings for MTO on SAPO-34 crystal at 600 K (Fig. 6b), which demonstrates again that HCP species formation follows the same pathway i.e. methylations for both catalyst materials, and the outer rim has a higher concentration of methanol [21]. However, the active rim is thicker in the case of SSZ-13, which is likely due to its less acid site density. Less acid site density leads to a lower density of formed HCP species, thus a better accessibility of the crystal can be obtained. Therefore, the size of active zone in a single crystal can be governed by the acid site density, further affecting the catalytic performance of the material.

When performing ETO reaction at 509 K over SSZ-13 (Fig. 6c), the fluorescent signal was detected in the outer rim of the crystal at the beginning of the reaction, and it moves inwards with time-on-stream, where the intergrowth structure is clearly visible in a same fashion as for SAPO-34 (Fig. 6d). This proves again that the fluorescent species are formed from mobile olefins in both catalyst materials [21]. After 15 min on-stream, the pattern for the SSZ-13 crystal is less homogeneous than the one for the SAPO-34 crystal, which might be due to its lower acid site density and consequently a lower reaction rate of olefins condensation. The confocal fluorescence microscopy measurements illustrate that acid site density influences the distribution and amount of formed HCP species within single crystals.

3.4. In situ infrared micro-spectroscopy

In a final part of our combined micro-spectroscopy investigation we aimed to gain more insight into chemical nature of the HCP species formed within individual SSZ-13 and SAPO-34 crystals during MTO and ETO. For this purpose, we have employed synchrotron-based IR micro-spectroscopy, which provides spectroscopic

Please cite this article in press as: Q. Qian, et al., Single-catalyst particle spectroscopy of alcohol-to-olefins conversions: Comparison between SAPO-34 and SSZ-13, Catal. Today (2013), http://dx.doi.org/10.1016/j.cattod.2013.09.056

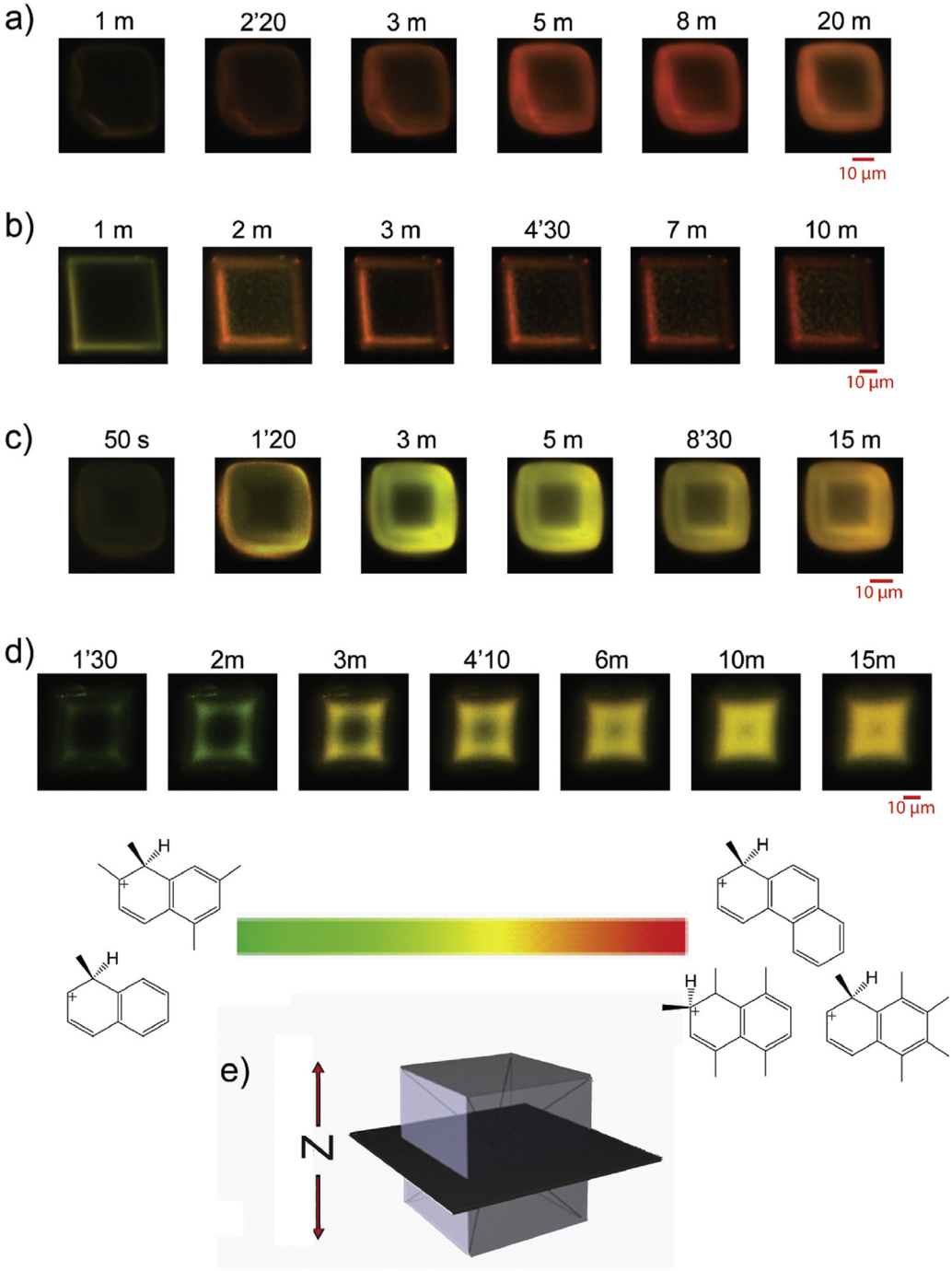

Fig. 6. Confocal fluorescence microscopy images during the methanol-to-olefins (MTO) reaction with time-on-stream at 600 K over (a) an individual 40 μm-sized SSZ-13 crystal and (b) an individual 50 μm-sized SAPO-34 crystal (Figure adapted from Ref. [21]). Confocal fluorescence microscopy images during the ethanol-to-olefins (ETO) reaction with time-on-stream at 509 K over (c) an individual 40 μm-sized SSZ-13 crystal and (d) an individual 50 μm-sized SAPO-34 crystal (figure adapted from Ref. [21]). (e) Schematics of the crystal, the plane represents where the measurements have been performed. The colors shown in the figure represent the fluorescence originated from two laser lines with an excitation of 488 nm (detection at 510–550 nm) and 561 nm (detection 565–635 nm).

fingerprints of the type and amount of aromatic and aliphatic hydrocarbons formed, as well as of the hydroxyl groups interacting with the encaged organic molecules at the single particle level [21].

Fig. 7 compares the IR spectra obtained for an individual activated SSZ-13 crystal before and after three pulses of methanol and ethanol at 553 K, respectively. For sake of better comparison, the IR spectra taken before and after same reactions for SAPO-34 crystal are also included [21]. The IR spectra were taken from a spot size of $20 \times 20\ \mu m^2$ in the center of the crystal. One can now consider three important regions in the measured IR spectra, i.e., the O—H stretching vibration region (>3500 cm^{-1}), the C—H stretching vibration region (2800–3100 cm^{-1}) and the C=C stretching and C—H deformation vibration region (1350–1650 cm^{-1}) [21]. As can be concluded from Fig. 7a, the SSZ-13 crystal has Brønsted acidity with two characteristic bands located at ~3600 and 3575 cm^{-1}, while the band at ~3730 cm^{-1} is assigned to silanol groups. The sharpness of the O—H band at 3595 cm^{-1} for SAPO-34, shown in Fig. 7a', and the absence of other bands in the OH stretching vibration region suggest that silicon is homogeneously distributed [21]. Additionally, the higher intensity of the O—H band at 3595 cm^{-1} correlates

Please cite this article in press as: Q. Qian, et al., Single-catalyst particle spectroscopy of alcohol-to-olefins conversions: Comparison between SAPO-34 and SSZ-13, Catal. Today (2013), http://dx.doi.org/10.1016/j.cattod.2013.09.056

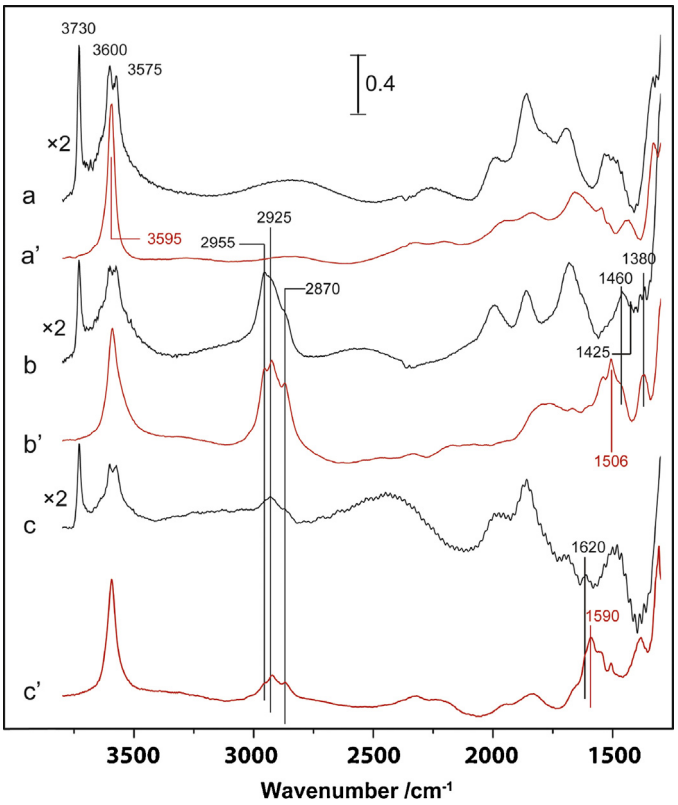

Fig. 7. Synchrotron-based IR spectra of an individual 40 μm-sized SSZ-13 crystal (a) before alcohol-to-olefins (ATO) reaction, (b) after three pulses of methanol, and (c) after three pulses of ethanol at 553 K. Synchrotron-based IR spectra of an individual 50 μm-sized SAPO-34 crystal (a′) before reaction, (b′) after three pulses of methanol, and (c′) after three pulses of ethanol at 553 K (Figures a′, b′, and c′ are adapted from Ref. [21]). The IR signal in the case of SSZ-13 is multiplied by a factor of 2.

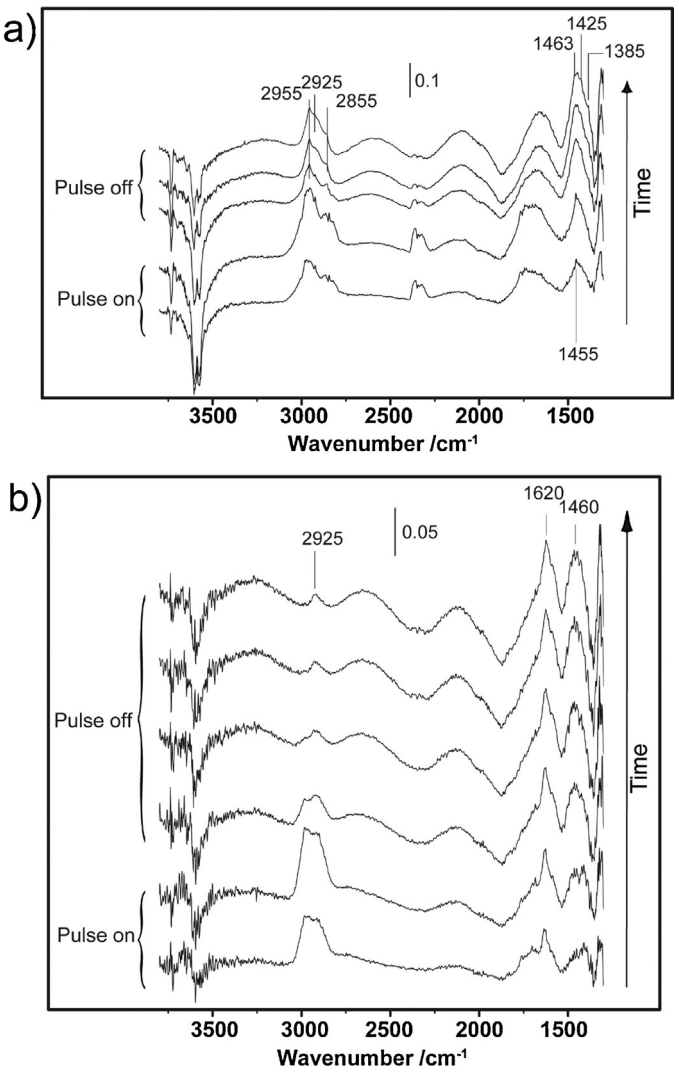

Fig. 8. (a) Subtracted synchrotron-based IR spectra from reaction during the first pulse of methanol over an individual 40 μm-sized SSZ-13 crystal at 553 K, the pulse lasted for 1 min and 20 s, and the interval of the displayed spectra is 40 s during the pulse and 1 min after the pulse. (b) Subtracted IR spectra from the first pulse of ethanol over an individual 40 μm-sized SSZ-13 crystal at 553 K, the pulse lasted for 1 min 20 s, and the interval of the displayed spectra is 40 s during the pulse and 1 min after the pulse.

with a higher acid site density as compared to SSZ-13, which is in line with the NH_3-TPD results, discussed above. After performing the ATO reactions, all IR bands in the O—H region decrease, which indicates a loss of the Brønsted acid sites in both catalyst materials as well as in the silanol groups in the SSZ-13 crystal. The loss of those species is strongly attributed to the formation of protonated HCP species as well as alkoxy groups. For the IR bands in the C—H stretching region, three bands centered at around 2955, 2925 and 2870 cm^{-1} appear during ATO reactions on both SAPO-34 and SSZ-13. They are representative for the formation of alkyl groups on aromatic rings [16]. Furthermore, when comparing MTO and ETO, a much more pronounced C—H stretching region is observed in the MTO reaction than in the ETO for both catalyst materials. Hence, one can conclude that there is a higher alkylation degree of the HCP species during MTO than during ETO on both crystals, which is due to the different formation paths for MTO and ETO as reported previously from our group [21].

If we compare the same ATO reaction on SSZ-13 and SAPO-34 crystals, the differences are also clear. The intensity in the aliphatic C-H region is higher for the SAPO-34 than SSZ-13 crystals, which suggests that more alkylated HCP species are formed on SAPO-34 most probably due to its higher acid site density. Moreover, in the C=C vibration and C—H deformation stretching region, for MTO (Fig. 7b and b′), the bands at ~1460 cm^{-1} and 1380 cm^{-1} can be found in both catalyst materials, which are most likely due to the C=C ring skeletal vibration of aromatics and bending vibration of methyl groups on benzenes, respectively [46,47]. This means that the active HCP species in both catalyst materials are methylated benzenes. However, an additional band in this region (~1425 cm^{-1} for SSZ-13 and ~1506 cm^{-1} band for SAPO-34) suggests the formation of distinct HCP species (e.g., different positions of alkyl groups or different number of rings) owing to their distinct activity i.e. acid strength.

For ETO (Fig. 7c and c′), the 1620 cm^{-1} band is observed for both cases, while one additional pronounced band at around 1590 cm^{-1} is evident for the SAPO-34 crystal. The former band is ascribed to the ring carbon–carbon skeletal vibrations for aromatics and the latter band is typical where the aromatic ring is conjugated further, e.g. PA molecules [47]. This shows that HCP species have a more conjugated nature in case of SAPO-34, which is in line with UV–vis results as more PA species formed in SAPO-34 due to its higher acid site density.

Fig. 8a and b displays the evolution of the synchrotron-based IR spectra in a single SSZ-13 crystal in the first pulse during MTO and ETO in more detail. The pulse for both cases lasted for 1 min and 20 s, and the IR spectra were taken every 40 s during the pulse and 1 min after the pulse in both cases. During the pulse of methanol, a decrease of Brønsted acidity and amount of silanol groups was observed, meanwhile two IR bands at ~1455 cm^{-1} and ~2978 cm^{-1} (similar as for SAPO-34 crystal [21]) rise at the beginning of the

Please cite this article in press as: Q. Qian, et al., Single-catalyst particle spectroscopy of alcohol-to-olefins conversions: Comparison between SAPO-34 and SSZ-13, Catal. Today (2013), http://dx.doi.org/10.1016/j.cattod.2013.09.056

MTO, indicating that the reaction is taking place. These two bands are most likely due to the formation of methoxy groups (methyl deformation mode and stretching vibration mode), which contribute to the removal of the acid sites at the early stage of the MTO reaction [48,49]. When the pulse is off, the two bands disappear and the acid sites are partially recovered. Interestingly, the intensity of the silanol groups remains the same after switching off the methanol flow, indicating that only methoxy species generated from Brønsted acid sites are reactive. As a result of the depletion of methoxy species, several new bands are formed. Specifically, two bands located at ~1463 and 1385 cm^{-1}, are indicative for the formation of methylated benzenes as discussed above [46]. The IR band at ~2925 cm^{-1} is assigned to the stretching vibration of the C—H bond from alkyl groups on aromatics [46]. In addition, the 1425 cm^{-1} band is likely originated from C—H bending vibration of methylated aromatic carbocations. It is reasonable to propose that the new species i.e. methylbenzenes are HCP molecules generated via methylation reactions, as evidenced from the previously described UV–vis results. These methylated benzene carbocations are therefore responsible for the absorption at ~400 nm in UV–vis spectra as discussed in detail in our previous work [21].

In the case of synchrotron-based IR data for ETO, as illustrated in Fig. 8b, a slight decrease is observedin the amount of both Brønsted acid sites and silanol groups when the pulse starts. Interestingly, the slow decrease in Brønsted acidity continues when the pulse is off and suggests that the formation of the protonated HCP species in the ETO process is not related to surface species created exclusively at Brønsted acid sites. The same behavior was also observed for SAPO-34 during ETO [21]. The lower decreasing rate of Brønsted acidity for SSZ-13, which corresponds with less HCP species formation as shown in the UV–vis spectra, is due to its lower acid site density. In addition, for the SSZ-13 crystal an absorption band at around 1620 cm^{-1} appears at the beginning of the reaction, and continuously increases even in the absence of ethanol. This band has been assigned to ν(C=C) modes of a complex mixture of carbonaceous, e.g. aromatic species [33,50,51], which is formed from condensation of olefins. At the end of the first pulse, bands at ~2925 and 1460 cm^{-1}, similar to the ones from MTO yet with much lower intensities, suggest the formation of alkylated aromatic species.

4. Conclusions

The catalytic performance of individual micron-sized SSZ-13 and SAPO-34 crystals have been compared during methanol-to-olefins (MTO) and ethanol-to-olefins (ETO) reactions by a combination of three micro-spectroscopy techniques. More specifically, UV–vis micro-spectroscopy has been applied to follow the formation of two distinct HCP species (i.e., markers of an active and a deactivating species) in a quantitative manner as a function of reaction time and temperature. In addition, confocal fluorescence microscopy has been used to unravel the spatiotemporal distribution of formed HCP species within one crystal. Finally, synchrotron-based IR micro-spectroscopy provided insight into the molecular structure and amount of the HCP species as well as the interactions of these molecules with the acid sites.

It was found that the SAPO-34 and SSZ-13 crystals are very similar MTO and ETO catalyst materials when comparing the nature of the formed HCP species as well as the formation pathways of these species. The formation of the most active HCP species, i.e., poly-alkylated benzene (PAB) carbocations, as characterized by an absorption band at around 400 nm band, was studied and fitted with first-order kinetics. In the case of MTO, it was found that the methylation reactions are responsible for PAB formation in both SAPO-34 and SSZ-13, whilst for ETO olefin condensation is governing the overall process. This is in agreement with the IR micro-spectroscopy data as the HCP species formed during MTO has a higher degree of alkylation than those observed during ETO. Moreover, the deactivating species, e.g. poly aromatic (PA) carbocations, as characterized by an absorption band at around 580 nm, was also studied in a quantitative way. It was found that the PA species are most likely formed at the expense of PAB species for both crystals during MTO, more specifically from methylation followed by condensation of PAB carbocations; while this is not the case for the ETO process as olefins condensation is more likely. Confocal fluorescence microscopy images show that the formed PA species are mainly located in the outer rim of the SAPO-34 and SSZ-13 crystals during the MTO process at 600 K, thus blocking the reactant molecules from diffusing into the inner part of the crystals. In contrast, the formation of the PA species during ETO involves the diffusion of reactants, e.g. mobile olefins, as the crystal intergrowth structures are clearly seen for both SAPO-34 and SSZ-13.

Based on our characterization data we can conclude that SAPO-34 and SSZ-13 also show different reactivity during both MTO and ETO. Furthermore, this difference comes from their distinct acid strength as well as their acid site density. In the case of MTO, a much lower E_a value with respect to the PAB formation for SSZ-13 than SAPO-34 indicates that acid strength plays an important role in this process. In addition, SSZ-13 deactivates faster in the low temperature region (below 563 K), and it possesses the highest PA/PAB ratio at 518 K. In contrast, for SAPO-34, the temperature for the highest PA/PAB ratio shifts to a higher temperature (576 K). This temperature shift can also be explained by the higher acid strength of SSZ-13. Moreover, the confocal fluorescence microscopy images show a larger active zone for SSZ-13 than SAPO-34. This can be rationalized by its lower acid site density, which influence the number and distribution of formed HCP species and furthermore may have impact on its catalytic performance.

In the case of ETO, comparable E_a values were found with respect to the formation of PAB for both crystals. This suggests that olefins condensation, which is the major source to produce PAB carbocations, is not affected by acid strength. In addition, a faster PAB formation was observed for all the measured temperatures for SAPO-34, which possesses a higher acid site density thus favoring condensation reactions. When comparing the PA content and PA/PAB ratio at temperatures lower than 600 K, an increasing trend with increasing reaction temperatures was observed for both crystals. However, SAPO-34 contains more PA species than SSZ-13, although the acid strength of the former material is lower. This is evidenced by (a) the more pronounced 580 nm absorption band in the UV–vis spectra and (b) an additional band at around 1590 cm^{-1} in the IR spectra. A plausible explanation could be the higher acid site density of SAPO-34, which favors the condensation reactions that are likely the major route contributing to both PAB and PA formation.

Acknowledgements

This research work is funded by the Netherlands Research School Combination-Catalysis (NRSC-C) and the Deanship of Scientific Research (DSR) of King Abdulaziz University, Jeddah under grant number (T-002-431). The authors gratefully acknowledge DSR for technical and financial support. We also acknowledge SOLEIL for access to the synchrotron radiation facilities under proposal number 20120471 and we would like to thank Dr. Frédéric Jamme and Dr. Paul Dumas for their kind help and discussions. Dr. Jan Kornatowski (Max Planck Institute, Mulheim, Germany) and Dr. Einar A. Eilertsen (University of Oslo, Norway) are acknowledged for providing the SAPO-34 and SSZ-13 crystals, respectively. Javier Ruiz-Martinez (Utrecht University, the Netherlands) also acknowledges CW-NWO for his VENI grant.

Please cite this article in press as: Q. Qian, et al., Single-catalyst particle spectroscopy of alcohol-to-olefins conversions: Comparison between SAPO-34 and SSZ-13, Catal. Today (2013), http://dx.doi.org/10.1016/j.cattod.2013.09.056

References

[1] U. Olsbye, S. Svelle, M. Bjørgen, P. Beato, T.V.W. Janssens, F. Joensen, S. Bordiga, K.P. Lillerud, Angew. Chem. Int. Ed. 51 (2012) 5810–5831.
[2] K. Hemelsoet, J. Van der Mynsbrugge, K. De Wispelaere, M. Waroquier, V. Van Speybroeck, ChemPhysChem 14 (2013) 1526–1545.
[3] M. Stöcker, Microporous Mesoporous Mater. 29 (1999) 3–48.
[4] J. Rass-Hansen, H. Falsig, B. Jørgensen, C.H. Christensen, J. Chem. Technol. Biotechnol. 82 (2007) 329–333.
[5] V. Van Speybroeck, K. Hemelsoet, K. De Wispelaere, Q. Qian, J. Van der Mynsbrugge, B. De Sterck, B.M. Weckhuysen, M. Waroquier, ChemCatChem 5 (2013) 173–184.
[6] C.D. Chang, A.J. Silvestri, J. Catal. 47 (1977) 249–259.
[7] M. Stöcker, Angew. Chem. Int. Ed. 47 (2008) 9200–9211.
[8] J.Q. Chen, A. Bozzano, B. Glover, T. Fuglerud, S. Kvisle, Catal. Today 106 (2005) 103–107.
[9] F. Bleken, M. Bjørgen, L. Palumbo, S. Bordiga, S. Svelle, K.-P. Lillerud, U. Olsbye, Top. Catal. 52 (2009) 218–228.
[10] S. Bordiga, L. Regli, D. Cocina, C. Lamberti, M. Bjørgen, K.P. Lillerud, J. Phys. Chem. B 109 (2005) 2779–2784.
[11] I.M. Dahl, S. Kolboe, J. Catal. 149 (1994) 458–464.
[12] I.M. Dahl, S. Kolboe, Catal. Lett. 20 (1993) 329–336.
[13] M. Bjørgen, S. Svelle, F. Joensen, J. Nerlov, S. Kolboe, F. Bonino, L. Palumbo, S. Bordiga, U. Olsbye, J. Catal. 249 (2007) 195–207.
[14] M. Bjørgen, U. Olsbye, D. Petersen, S. Kolboe, J. Catal. 221 (2004) 1–10.
[15] A.K. Talukdar, K.G. Bhattacharyya, S. Sivasanker, Appl. Catal. A: Gen. 148 (1997) 357–371.
[16] F.F. Madeira, N.S. Gnep, P. Magnoux, S. Maury, N. Cadran, Appl. Catal. A: Gen. 367 (2009) 39–46.
[17] R. Johansson, S. Hruby, J. Rass-Hansen, C. Christensen, Catal. Lett. 127 (2009) 1–6.
[18] B. Arstad, S. Kolboe, J. Am. Chem. Soc. 123 (2001) 8137–8138.
[19] S. Svelle, F. Joensen, J. Nerlov, U. Olsbye, K.-P. Lillerud, S. Kolboe, M. Bjørgen, J. Am. Chem. Soc. 128 (2006) 14770–14771.
[20] W. Song, J.F. Haw, J.B. Nicholas, C.S. Heneghan, J. Am. Chem. Soc. 122 (2000) 10726–10727.
[21] Q. Qian, J. Ruiz-Martínez, M. Mokhtar, A.M. Asiri, S.A. Al-Thabaiti, S.N. Basahel, H.E. van der Bij, J. Kornatowski, B.M. Weckhuysen, Chem. Eur. J. 19 (2013) 11204–11215.
[22] J. Haw, D. Marcus, Top. Catal. 34 (2005) 41–48.
[23] H. Fu, W. Song, J. Haw, Catal. Lett. 76 (2001) 89–94.
[24] E.E. Wolf, F. Alfani, Catal. Rev. Sci. Eng. 24 (1982) 329–371.
[25] S. Bhatia, J. Beltramini, D.D. Do, Catal. Rev. Sci. Eng. 31 (1989) 431–480.
[26] M. Guisnet, P. Magnoux, Appl. Catal. A: Gen. 212 (2001) 83–96.
[27] M. Guisnet, L. Costa, F.R. Ribeiro, J. Mol. Catal. A: Chem. 305 (2009) 69–83.
[28] L. Karwacki, E. Stavitski, M.H.F. Kox, J. Kornatowski, B.M. Weckhuysen, Angew. Chem. Int. Ed. 46 (2007) 7228–7231.
[29] E.A. Eilertsen, M.H. Nilsen, R. Wendelbo, U. Olsbye, K.P. Lillerud, Stud. Surf. Sci. Catal. 174 (2008) 265–268.
[30] S. Ashtekar, S.V.V. Chilukuri, D.K. Chakrabarty, J. Phys. Chem. 98 (1994) 4878–4883.
[31] Q. Zhu, J.N. Kondo, T. Tatsumi, S. Inagaki, R. Ohnuma, Y. Kubota, Y. Shimodaira, H. Kobayashi, K. Domen, J. Phys. Chem. C 111 (2007) 5409–5415.
[32] D. Mores, E. Stavitski, M.H.F. Kox, J. Kornatowski, U. Olsbye, B.M. Weckhuysen, Chem. Eur. J. 14 (2008) 11320–11327.
[33] L. Palumbo, F. Bonino, P. Beato, M. Bjørgen, A. Zecchina, S. Bordiga, J. Phys. Chem. C 112 (2008) 9710–9716.
[34] D. Mores, J. Kornatowski, U. Olsbye, B.M. Weckhuysen, Chem. Eur. J. 17 (2011) 2874–2884.
[35] D.M. McCann, D. Lesthaeghe, P.W. Kletnieks, D.R. Guenther, M.J. Hayman, V. Van Speybroeck, M. Waroquier, J.F. Haw, Angew. Chem. Int. Ed. 47 (2008) 5179–5182.
[36] M. Bjørgen, F. Bonino, S. Kolboe, K.-P. Lillerud, A. Zecchina, S. Bordiga, J. Am. Chem. Soc. 125 (2003) 15863–15868.
[37] K. Hemelsoet, Q. Qian, T. De Meyer, K. De Wispelaere, B. De Sterck, B.M. Weckhuysen, M. Waroquier, V. Van Speybroeck, Chem. Eur. J. (2013), http://dx.doi.org/10.1002/chem.201301965.
[38] W. Song, H. Fu, J.F. Haw, J. Phys. Chem. B 105 (2001) 12839–12843.
[39] D.M. Marcus, W. Song, L.L. Ng, J.F. Haw, Langmuir 18 (2002) 8386–8391.
[40] D. Lesthaeghe, A. Horré, M. Waroquier, G.B. Marin, V. Van Speybroeck, Chem. Eur. J. 15 (2009) 10803–10808.
[41] I.M. Dahl, H. Mostad, D. Akporiaye, R. Wendelbo, Microporous Mesoporous Mater. 29 (1999) 185–190.
[42] A.G. Gayubo, A. Alonso, B. Valle, A.T. Aguayo, J. Bilbao, AIChE J. 58 (2012) 526–537.
[43] H. Schulz, Catal. Today 154 (2010) 183–194.
[44] J. Ruiz-Martínez, I.L.C. Buurmans, W.V. Knowles, D. van der Beek, J.A. Bergwerff, E.T.C. Vogt, B.M. Weckhuysen, Appl. Catal. A: Gen. 419–420 (2012) 84–94.
[45] I.L.C. Buurmans, J. Ruiz-Martínez, W.V. Knowles, D. van der Beek, J.A. Bergwerff, E.T.C. Vogt, B.M. Weckhuysen, Nat. Chem. 3 (2011) 862–867.
[46] J.W. Park, G. Seo, Appl. Catal. A: Gen. 356 (2009) 180–188.
[47] G. Socrates, Infrared and Raman Characteristic Group Frequencies: Tables and Charts, Third ed., John Wiley & Sons Ltd, Chichester, 2001.
[48] H. Yamazaki, H. Shima, H. Imai, T. Yokoi, T. Tatsumi, J.N. Kondo, Angew. Chem. Int. Ed. 50 (2011) 1853–1856.
[49] T.R. Forester, R.F. Howe, J. Am. Chem. Soc. 109 (1987) 5076–5082.
[50] M. Rozwadowski, M. Lezanska, J. Wloch, K. Erdmann, R. Golembiewski, J. Kornatowski, Chem. Mater. 13 (2001) 1609–1616.
[51] H.G. Karge, W. Nießxen, H. Bludau, Appl. Catal. A: Gen. 146 (1996) 339–349.

Please cite this article in press as: Q. Qian, et al., Single-catalyst particle spectroscopy of alcohol-to-olefins conversions: Comparison between SAPO-34 and SSZ-13, Catal. Today (2013), http://dx.doi.org/10.1016/j.cattod.2013.09.056